The Journal of Chemical Physics

Melts of nonconcatenated rings in spherical confinement

Cite as: J. Chem. Phys. **153**, 064903 (2020); https://doi.org/10.1063/5.0013929
Submitted: 15 May 2020 . Accepted: 20 July 2020 . Published Online: 10 August 2020

Stanard Mebwe Pachong, Iurii Chubak, Kurt Kremer, and Jan Smrek

The Journal of Chemical Physics ARTICLE scitation.org/journal/jcp

Melts of nonconcatenated rings in spherical confinement

Cite as: J. Chem. Phys. 153, 064903 (2020); doi: 10.1063/5.0013929
Submitted: 15 May 2020 • Accepted: 20 July 2020 •
Published Online: 10 August 2020

Stanard Mebwe Pachong,[1,a] Iurii Chubak,[2,b] Kurt Kremer,[1,c] and Jan Smrek[2,d]

AFFILIATIONS

[1] Max Planck Institute for Polymer Research, Ackermannweg 10, 55128 Mainz, Germany
[2] Faculty of Physics, University of Vienna, Boltzmanngasse 5, A-1090 Vienna, Austria

[a] pachong@mpip-mainz.mpg.de
[b] Author to whom correspondence should be addressed: iurii.chubak@univie.ac.at
[c] kremer@mpip-mainz.mpg.de
[d] jan.smrek@univie.ac.at

ABSTRACT

Motivated by the chromosomes enclosed in a cell nucleus, we study a spherically confined system of a small number of long unknotted and nonconcatenated polymer rings in a melt and systematically compare it with the bulk results. We find that universal scaling exponents of the bulk system also apply in the confined case; however, certain important differences arise. First, due to confinement effects, the static and threading properties of the rings depend on their radial position within the confining sphere. Second, the rings' dynamics is overall subdiffusive, but anisotropic along the directions parallel and perpendicular to the sphere's radius. The radial center of mass displacements of the rings are in general much smaller than the angular ones, which is caused by the confinement-induced inhomogeneous radial distribution of the whole rings within the sphere. Finally, we find enhanced contact times between rings as compared to the bulk, which indicates slow and predominantly coordinated pathways of the relaxation of the system.

I. INTRODUCTION

Nonconcatenated and unknotted ring polymer melts have been fascinating physicists for years, and still a complete understanding of their properties is lacking. Static properties of linear chains in melt are to a good approximation Gaussian,[1] and dynamic properties are well-described by tube and reptation theories.[2,3] However, joining the two ends of each chain, while keeping the created rings unknotted and nonconcatenated, makes it difficult to treat the system with analytical techniques.[4] Therefore, different theoretical models have been developed to tackle the problem under simplifying assumptions, such as treating a ring as in the lattice of fixed obstacles formed by the other rings,[5–9] assuming tree-like conformations,[10–12] or various other.[13–15] Along these ideas, computer simulations[13,16–22] have been an indispensable tool for testing the assumptions and verifying the experimental results[23–32] under perfectly controlled conditions. This joint effort has proven to be successful and has generated a range of interesting results that highlight how permanent topological constraints of rings impact equilibrium properties, which turned out to be dramatically different from their linear counterparts. In particular, the melt of rings exhibits a power-law stress relaxation modulus with the absence of the rubbery plateau typical for the linear polymer melts.[19,23] Rings, significantly longer than the entanglement length N_e, adopt compact conformations characterized by the scaling relation $R \sim N^{\nu}$ between their mean size R and their polymerization degree N with the exponent $\nu = 1/d = 1/3$, where $d = 3$ is the dimension of the space. Furthermore, the probability of two monomers separated by the contour distance s being in mutual proximity in space is also a power-law $P(s) \sim s^{-\gamma}$ with the exponent $\gamma \simeq [1.05, 1.17]$.[18,21] The values of the exponents $\nu = 1/3$ and γ close to unity

describe the so-called crumpled (fractal) globule ensemble that characterizes melts of long polymers under unknotted and uncrossable topological constraints.

The above-mentioned conformational properties and the corresponding exponent values have sparked further motivation to study these systems in the context of genome folding. The fractal globule model is consistent with the population average ensemble of the chromatin fiber configurations in cell nuclei of higher eukaryotes.[8,34–36] In contrast to rings, the chromosomes do have ends, but the rationale behind such connection is the slow chromosomal reptational relaxation mechanism. Due to temporary topological constraints, the reptation is much slower than the relevant biological time scales.[36] If the chromatin fiber is mostly uncrossable with very slow or inhibited reptation but otherwise random, the crumpled globule ensemble arises naturally. An account of topological constraints has proven to be useful in finding detailed genome conformations from experimental data.[37]

Nevertheless, the above-outlined correspondence is based on the results of bulk simulations of many rings subject to periodic boundary conditions. Chromatin fiber, on the other hand, is confined in the nucleus and, in the case of human diploid cells, consists of 46 chromosomes only. Hence, the majority of chromosomes is affected by the confinement geometry, and their conformations result from the competition between the confinement and the compression due to topological constraints. In this direction, the work[38] studied a single long ring in cubic confinement and found that the conformations of the ring's subchains are consistent with the crumpled globule picture in terms of $\nu = 1/3$ but found $\gamma \simeq 0.9$. The value of $\gamma < 1$ cannot be a true asymptotic value of the exponent for conformations with $\nu = 1/3$ because $1 \leq \gamma \leq 1 + \nu$ for geometric reasons as detailed in Refs. 35 and 39. No dynamics was reported in Ref. 38, as the simulations had been carried out using Monte Carlo sampling with non-local moves. Single ring static properties have also been investigated in biaxial confining geometry, which leads to the extension of the ring in the third dimension, markedly different from a linear confined chain.[40–42] The impact of a cylindrical confinement on the static properties of semiflexible rings has been studied experimentally in Ref. 32. In contrast to the approximate view of the rings as tree-like objects, that work confirms significant inter-ring threadings observed previously in the bulk simulations.[43–45] The model-independent threading differences between the effective tree-like model[21] and the accurate molecular dynamics simulations have been quantitatively analyzed in Ref. 46.

Here, we investigate the impact of confinement, ring topology, and a small number of polymer chains on static and dynamic properties of the system. We simulate a spherically confined set of $M = 46$ rings of lengths $N = 200$, 400, 800, and 1600 with the same model parameters as in Ref. 18 detailed below (see the system snapshot in Fig. 1). We find and characterize global structural organization of the confined rings as well as differences in their single chain static properties with respect to the bulk results. Additionally, we report mean inter-ring threading properties, which are important for the dynamics of systems with long rings.[44,47–53] We find that they are similar to the bulk systems but vary with the rings' radial position within the confining sphere. Finally, we report dynamic properties of the system, which, *inter alia*, exhibit anisotropic mean-squared displacements of the ring's center of mass within the enclosing sphere caused by the confinement-induced density variations.

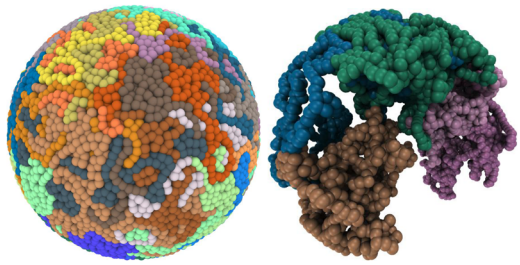

FIG. 1. System snapshots. Left panel: the system with $N = 800$ rings. Right panel: the same system when only five rings are shown. The compact and territorial ring arrangement can be observed.

II. MODEL

We used the well-known polymer model[54] in which the excluded volume interaction between any two monomers is described by a purely repulsive and shifted Lennard-Jones potential,

$$U_{\mathrm{LJ}}(r) = \left(4\varepsilon\left[\left(\frac{\sigma}{r}\right)^{12} - \left(\frac{\sigma}{r}\right)^{6}\right] + \varepsilon\right)\theta(2^{1/6}\sigma - r), \tag{1}$$

with $\theta(x)$ being the Heaviside step function. The polymer bonds were modeled by a finitely extensible nonlinear elastic (FENE) potential,

$$U_{\mathrm{FENE}}(r) = -\frac{1}{2}r_{\mathrm{max}}^2 K \log\left[1 - \left(\frac{r}{r_{\mathrm{max}}}\right)^2\right], \tag{2}$$

where $K = 30.0\varepsilon/\sigma^2$ and $r_{\mathrm{max}} = 1.5\sigma$. These parameters make the chains essentially uncrossable. Additionally, we used the angular bending potential

$$U_{\mathrm{angle}} = k_\theta(1 - \cos(\theta - \pi)), \tag{3}$$

with $k_\theta = 1.5\varepsilon$ to induce higher stiffness that corresponds to a lower entanglement length $N_e = 28 \pm 1$ at the studied monomer density $\rho = 0.85\sigma^{-3}$.[55] The ring lengths therefore correspond to the range from 7 to 57 entanglement lengths. The interaction between monomers and the structureless confining sphere was also purely repulsive and given by $U_{\mathrm{LJ}}(R - r)$, where R is the radius of the sphere, r denotes here the distance between the monomer and the sphere's center, and U_{LJ} is the same as in (1). The simulations were performed in the NVT ensemble using the large-scale atomic/molecular massively parallel simulator (LAMMPS) engine[56] using the integration time step $\Delta t = 0.012\tau$, where $\tau = \sigma(m/\varepsilon)^{1/2}$. To maintain the constant temperature $T = 1.0\varepsilon$, all monomers were weakly coupled to a Langevin thermostat using a coupling constant $\gamma = 1.0\tau^{-1}$. The Langevin thermostat in spherical confinement induces stochastic values of angular momentum that can obscure the real dynamics. To prevent that, we zero the total angular momentum every ten steps by subtracting the appropriate value of the rotational component of the velocity of each

TABLE I. Size and shape properties of the confined rings. R is the radius of the confining sphere, $\langle R_g^2 \rangle$ is the mean-square radius of gyration, $\langle R_e^2 \rangle$ is the mean-square distance between two monomers separated by the contour length $N/2$, and λ_i, $i = 1, 2, 3$, are the eigenvalues of the gyration tensor ordered such that $\lambda_1 \geq \lambda_2 \geq \lambda_3$. The value in the parentheses indicates the standard error.

N	R/σ	$\langle R_g^2 \rangle/\sigma^2$	$\langle R_e^2 \rangle/\sigma^2$	$\langle \lambda_1 \rangle/\langle \lambda_3 \rangle$	$\langle \lambda_2 \rangle/\langle \lambda_3 \rangle$
200	13.72	26.4(0.2)	73.4(0.6)	5.64(0.04)	2.25(0.01)
400	17.29	44.4(0.7)	120.7(2.5)	5.24(0.08)	2.14(0.02)
800	21.78	73.1(1.1)	195.4(3.8)	4.93(0.10)	2.06(0.01)
1600	27.44	120.5(2.8)	320.2(10.4)	4.89(0.12)	2.03(0.02)

monomer. After the subtraction, the velocities are rescaled to maintain the set temperature. Performing this procedure every step is computationally more costly, and as we checked, this has no effect on the dynamics, as seen in Fig. S10 of the supplementary material.

A. System preparation

Initially, a set of M neighboring rings was extracted from the prepared bulk sample of Ref. 18 and placed in the confining sphere that just enclosed all rings. Then, a short ($\sim 10^4 \tau$) simulation was run to compress the sphere to reach the target monomer density. The confining sphere radius R is reduced in steps that are much shorter (about 1%) than the equilibrium bond length and thus allow thermalization and equilibration on local scales. The final values of R for each system are listed in Table I. After reaching the final density, the systems have been further equilibrated for over $10^6 \tau$ ($N = 200$ and $N = 400$) or $10^7 \tau$ ($N = 800$ and $N = 1600$). From Ref. 18 and by computing the radius of gyration autocorrelation function, we know that this is long enough to reach equilibrium. Additionally, we checked by computing the linking number between all pairs of rings that during the system preparation, the rings had not linked. Only afterward, production runs were run with a total duration over $2 \cdot 10^7 \tau$ for all N considered. Configurations were sampled every 1200τ.

III. RESULTS

A. Conformational properties

We characterize the ring's shape and size by computing the eigenvalues λ_i ($i = 1, 2, 3$, arranged as $\lambda_1 \geq \lambda_2 \geq \lambda_3$) of its gyration tensor,

$$G_{ij} = \frac{1}{N} \sum_{n=1}^{N} (r_i^{(n)} - R_i)(r_j^{(n)} - R_j), \tag{4}$$

where $r_i^{(n)}$ is the ith component of the position vector $\mathbf{r}^{(n)}$ of the nth monomer and $\mathbf{R}$ is the center of mass position of the ring. Then, the ring's mean-square radius of gyration $\langle R_g^2 \rangle$ can be computed as $\langle R_g^2 \rangle = \sum_{i=1}^{3} \langle \lambda_i \rangle$ with the brackets $\langle \cdots \rangle$ standing for the time and ensemble averaging. Certain population average conformational properties are listed in Table I. As shown in Fig. 2(a), both the confined and bulk systems of rings approach the scaling of the radius of gyration with N with exponent $\nu = 1/3$ [see also Fig. S1(a) for the scaling of eigenvalues and Fig. S2(c) for $\langle R_g^2 \rangle$ normalized by $N^{2/3}$]; however, the confined rings are on average 10%–15% smaller than their bulk counterparts [see the inset of Fig. 2(a)]. This shows that the compression due to topological constraints is "softer" than by the hard walls. Furthermore, as seen in Fig. 2(b), the normalized probability distributions of the rings' radius of gyration overlap fairly well for different polymerization degrees.

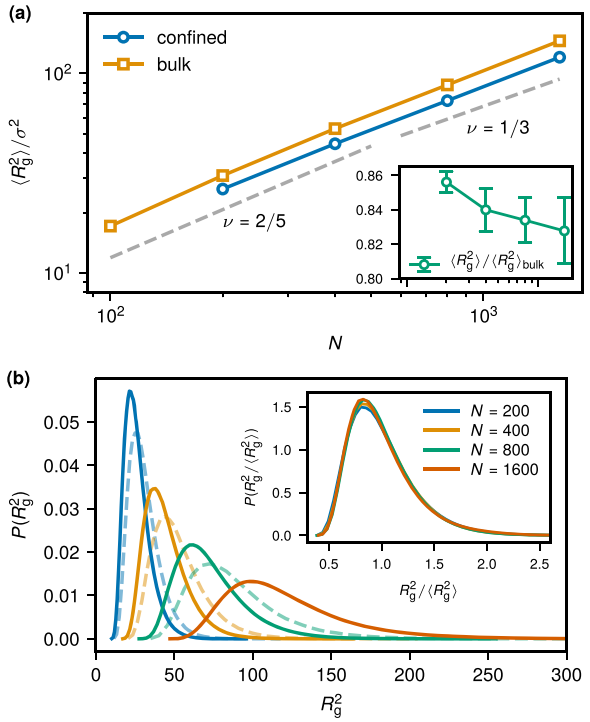

FIG. 2. Scaling of the confined rings' radius of gyration. (a) The mean-square radius of gyration $\langle R_g^2 \rangle$ as a function of the ring length N on a log–log scale for the bulk and the confined systems. The bulk data were adapted from Halverson *et al.*[18] The dashed lines represent power-laws with the marked exponents ν. Inset: relative decrease in the $\langle R_g^2 \rangle$ in the confined system with respect to the bulk one (x-axis is the same as in the main plot). (b) Probability distributions of $\langle R_g^2 \rangle$. Dashed curves of the same color correspond to the bulk systems. Inset: the same distributions as in the main plot but scaled by the mean.

Additionally, we probed the structure of the subchains of the rings by measuring the mean-squared internal distance $\langle d^2(s) \rangle$ for each segment length s as the squared distance between the endpoints of the segment averaged over the segments position within the ring and averaged over rings. It shows a range of various scaling regimes from the exponent 2 (straight segments below the persistence length) through 1 for random walk-like configurations to the exponent 2/3 characterizing the compact fractal structure (Fig. 3), in full analogy to the bulk results.[18]

As detailed later on in the text, the confinement in this relatively small system of rings causes significant structural rearrangements in comparison to the bulk that, as a consequence, have a pronounced effect on the rings' conformational properties with respect to their

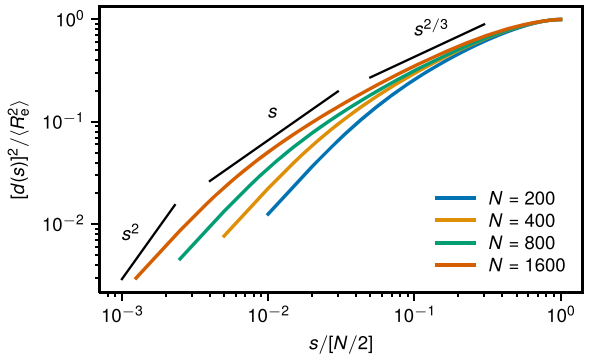

FIG. 3. Conformational properties of the subchains of the rings. Mean-square internal distance $\langle d^2(s)\rangle$, computed for each segment length s as the squared distance between the endpoints of the segment averaged over the segments position within the ring and averaged over rings. For each N, $\langle d^2(s)\rangle$ is normalized by the ring's mean-square end-to-end distance defined as $\langle R_e^2\rangle = \langle d^2(N/2)\rangle$.

radial position within the sphere. In particular, the rings located at the periphery tend to be more compact than the ones positioned more centrally, as shown in Fig. 4. To quantify this in more detail, we divided the rings into a subset of outer ones, whose center of mass is located at $r > 2R/3$, and inner ones, for which $r < 2R/3$. $2R/3$ is the median of the radial ring's distribution [see Fig. 8(a)]. We find that the size of outer rings, being closer to the bulk ones, is about 25% larger than the size of the inner ones. Both subsets approach the size scaling with $\nu = 1/3$ for larger N (see Fig. S2). This bias shows that the compression by an external potential and that by topological constraints are not equivalent. The external potential is sometimes used to model compact conformations when the topological constraints are neglected.[57] Moreover, from the eigenvalues of the gyration tensor, we compute a range of other shape parameters that are reported in the supplementary material (see Figs. S1–S4). For instance, we observe that the rings located closer to the confining wall are more aspherical and oblate (see Figs. S3–S4).

The contact probability $P(s)$ represents the probability that two monomers of a ring, separated by a contour distance s, are in contact in 3D space. It is computed for each segment length s as the fraction of times the segments endpoints are within a cutoff distance r_c averaged over the segments position within the rings and averaged over rings. We have found that $P(s)$ remains nearly unaffected by the confinement and, for bigger contour distances, scales as $P(s) \sim s^{-\gamma}$ with the scaling exponent $\gamma = 1.12 \pm 0.02$ (Fig. 5). The exponent γ is related through the relation $\gamma = 2 - \beta$ to another exponent β characterizing the scaling of the number of surface monomers of a segment $n_{\mathrm{surf}}(s) \sim s^{\beta}$.[18,35] The surface of a segment consists of monomers that neighbor the confining wall or monomers from other segments. For space-filling polymer conformations, that is the ones characterized by $\nu = 1/3$ in three dimensions, the exponent β also gives the fractal dimension d_b of the segment's surface by $d_b = \beta/\nu$. As opposed to the bulk system, the smooth confining wall induces $d_b = 2$ at least for some segments. The fact that we recovered the bulk value of γ suggests that the number of the segments with $d_b = 2$ is inferior to the other segments with higher d_b. Note that this is not a trivial consequence of the fact that the system size scales as $R \sim N^{1/3}$ because the segments aligning the wall smoothly could induce such a smooth surface also in other segments deeper inside the confining volume. We support the analysis by measuring directly the scaling of surface monomers. We find the value of the exponent $\beta = 0.95$ to be the same as in the bulk case.[18] We further looked if the smooth surfaces of the outer rings affect the properties of the single chain structure factor. As shown in Ref. 18, the structure factor of a segment of length s follows

$$S(q) \sim s^{\beta-1}/q^{(2-\beta)/\nu}. \tag{5}$$

See also Refs. 58 and 59 for a more refined discussion of this result. For $\beta = 1$ and $\nu = 1/3$, the scaling gives $S(q)q^3 \sim$ const, as evidenced by the plateau in Fig. 6(a). The inset highlights differences for the inner and outer rings, discriminated by their radial position with respect to $2R/3$ that is the median of the radial distribution [see Fig. 8(a)]. This difference could be attributed to smaller β of the outer rings due to partly smoother surface in comparison to

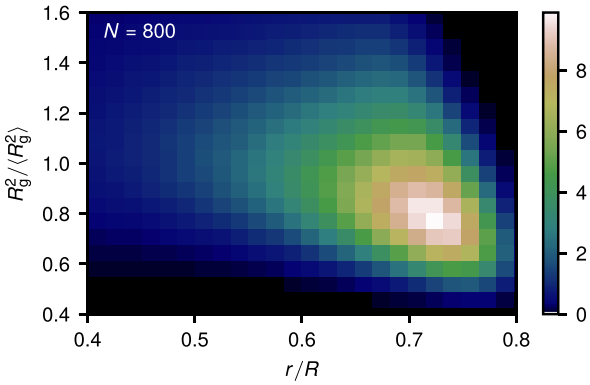

FIG. 4. Distribution of the rings' radius of gyration within the sphere. Probability density of finding a ring of size R_g with its center of mass located at a distance r from the center of the confining sphere of radius R for the system with $N = 800$. Other systems have very similar distributions (see Fig. S4).

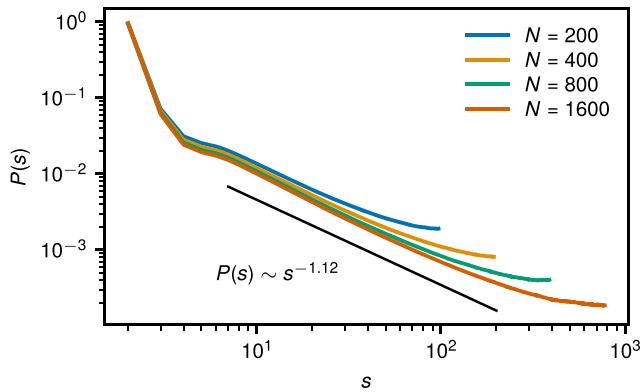

FIG. 5. Contact probability $P(s)$ as function of the segment length on a log–log scale. The power-law with the marked exponent value is consistent for all ring lengths. For computing $P(s)$, we used $r_c = 2^{1/6}\sigma$ (results for other values of r_c do not differ substantially).

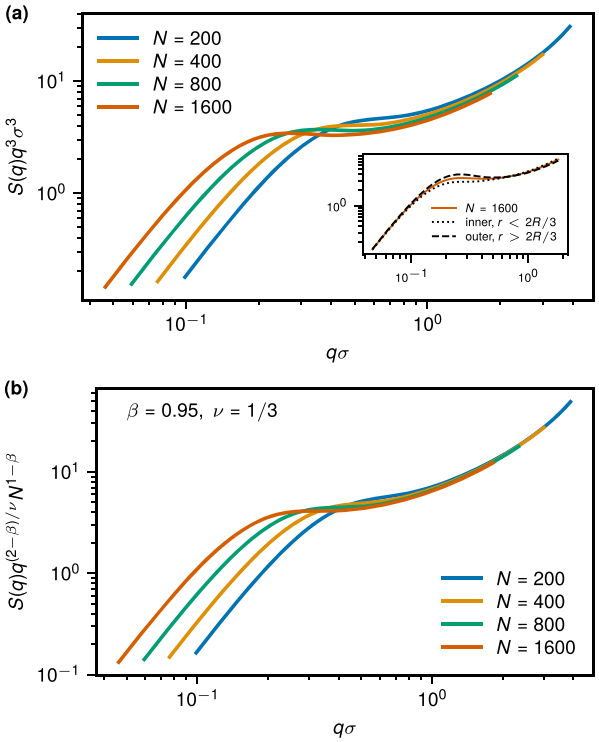

FIG. 6. The single-chain static structure factor. (a) $S(q)$ multiplied by q^3. Inset: $S(q)$ for $N = 1600$ differentiated by the radial position of rings. (b) $S(q)$ rescaled by $N^{1-\beta}q^{(2-\beta)/\nu}$ motivated by the relation (5).

the inner rings. It is, however, difficult to confirm this because the inner rings also show a bit more open conformations and, therefore, smaller effective ν at these scales. Another option is to consider the scaling of the contact probability for the outer and inner rings separately. In contrast, we systematically see the opposite trend with γ being smaller (and, therefore, β higher) for the outer rings (Fig. S7). Additionally, only for $N = 200$, γ of the outer rings is below unity and close to 0.9, which is consistent with the findings of Ref. 38. This is the consequence of the conformational change due to the presence of the wall, since it is not found for the inner or bulk rings. More work is necessary to determine the correct scaling of the structure factor and the contact probability for such "hybrid" conformations, where the surface roughness is affected by a smooth interface. Nevertheless, we get a better overall collapse of the structure factor (5) when $\beta \simeq 0.95$ is used [Fig. 6(b)], similar to the bulk results.[18] The remaining small inconsistency in the numerical verification of the theoretical relation $\gamma + \beta = 2$ is an open question noticed already for the bulk. A part can be attributed to finite-size scaling corrections.[18,58,59]

The presence of the confinement induces local monomer density variations in the wall's proximity (Figs. 7 and S8). The small differences between the different systems arise from the different curvature with respect to the local scale. More importantly, the confinement also significantly affects the global ring positioning within the sphere [Fig. 8(a)]. This shows very little variation for different

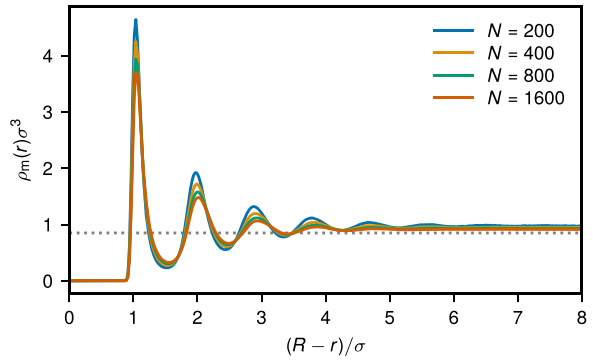

FIG. 7. Monomer density variations. Radial monomer density profiles as a function of the radial distance from the confining wall for systems with rings of different length N. The gray dashed line indicates the mean monomer density $\rho\sigma^3 = 0.85$.

N. Even at dilute conditions, ring polymers are stronger depletants than linear chains[42] due to enhanced effective repulsion between rings that stems from additional topological uncrossability constraints.[60,61] At high concentrations, the rings become compact due

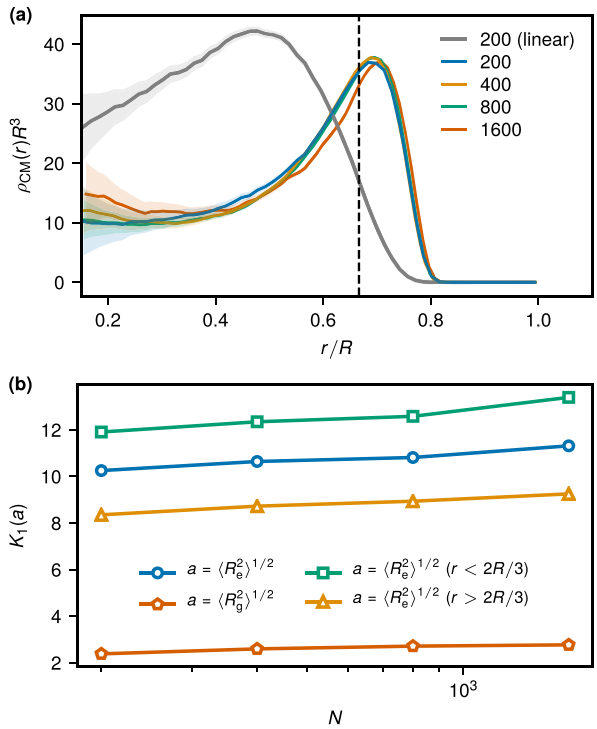

FIG. 8. Global system order. (a) Radial density profile (multiplied by R^3) of the ring's center of mass within the confining sphere of radius R. The gray line shows $\rho_{CM}(r)R^3$ for the melt of linear chains with $N = 200$ at the same mean monomer density $\rho\sigma^3 = 0.85$. In all cases, shaded regions indicate error bars. The black dotted line located at about $r = 2R/3$ indicates the median point of the radial rings' probability distribution within the sphere, $P_{CM}(r) = 4\pi r^2 \rho_{CM}(r)$. (b) The mean number of neighbors $K_1(a)$ of a ring for different threshold a values as a function of N. The green and yellow lines differentiate K_1 by the rings position within the sphere: inner rings are located at $r < 2R/3$, while outer ones at $r > 2R/3$.

to topological interactions, and their internal density distribution exhibits a deeper correlation hole in comparison to linear chains.[18] The rings are more compact at the wall, and therefore, their correlation hole there is even deeper. As a result, the fluid is more structured at the wall, similar to other effective colloidal particles such as multi-arm stars.[62] In the present system, the positional distribution of the rings' center of mass exhibits a single maximum of the radial distribution at about 2/3 of the radius from the sphere's center, while the density minimum close to the center of the sphere is much deeper than in the case of the linear chains. This effect arises from the compact conformation of the rings and their resulting deeper correlation hole. The density profiles collapse well on each other when the length scale is normalized by the confining radius R [see Fig. 8(a)], despite the fact that monomer density variations penetrate deeper into the sphere with decreasing N (see Fig. S8). To study relative arrangement of rings within the sphere, we measured their mean number of neighbors $K_1(a)$ [Fig. 8(b)]. Two rings are considered as neighbors if their centers of mass are located within a certain distance a. The mean values for the longest ring lengths are about 30% lower in comparison to the bulk systems.[18] This is mostly because of the rings located close to the wall ($r > 2R/3$), due to which they are missing about half of the possible neighbors with respect to the bulk. The inner rings ($r < 2R/3$) experience only about a 10% reduction, consistent with the size decrease in this region [Fig. 2(d)]. Here, we selected the threshold distance $2R/3$ because it represents the median of the ring positional distribution, that is, it is equally likely to find a ring in the regions with $r < 2R/3$ and $r > 2R/3$.

B. Threading properties

The rings cannot cross and therefore link, but they can thread as one ring pierces through the eye of another ring. The mutual ring threading is an important multi-ring property that due to the topological constraints is believed to strongly affect the dynamics of the system.[43,44,46–53,63,64] To analyze threadings, we have used the minimal surface approach. Each ring is considered as a fixed boundary on which a disc-like surface is spanned and subsequently minimized using a mean-curvature evolution, as detailed in Ref. 46. Then, the intersection of one ring's contour with another ring's minimal surface represents a threading. This approach has already been used to clarify the extent and the role of threadings in equilibrium bulk systems. Other approaches are also possible;[44,48] however, the minimal surfaces provide an intuitive geometric picture of the inter-ring threading, and moreover, the obtainable threading statistics is independent of the underlying polymer model.[46]

The threadings can be of various depth, which is characterized by the separation length L_{sep} defined as

$$L_{\mathrm{sep}} = \min\left(\sum_{i=\mathrm{even}} L_{\mathrm{t}_i}, \sum_{i=\mathrm{odd}} L_{\mathrm{t}_i}\right), \tag{6}$$

where L_{t_i} is the (threading) length between the ith and the $(i+1)$th penetrations of the surface (see Refs. 43 and 46 for details) and its ratio $Q = L_{\mathrm{sep}}/(N - L_{\mathrm{sep}})$, which describes the relative fraction of

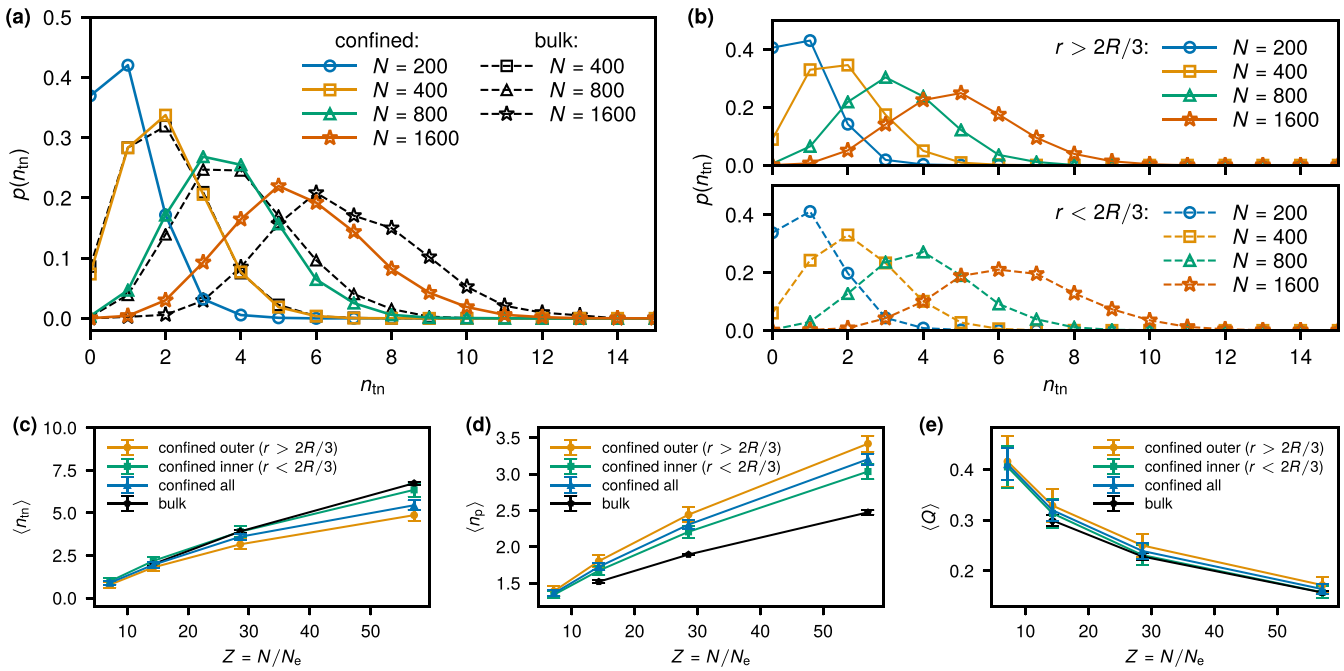

FIG. 9. Threading statistics. (a) Probability density of the number of the neighbors threaded by a single ring (see the main text for definition); comparison between the confined (colored lines) and bulk (black lines) systems. (b) Probability density of the number of the neighbors threaded by a single ring that has its center of mass located at $r > 2R/3$ (top panel) and $r < 2R/3$ (bottom panel). (c) Mean number of threaded neighbors as a function of the ring length computed from the distributions in the panels (a) and (b). (d) Mean number of surface penetrations as a function of N. (e) Mean values of Q as a function of N (see the main text for definition).

the threading ring length on the two sides of the threading ring's surface.

In Fig. 9(a), we report the distribution of the number of threaded neighbors for various ring lengths. We consider a ring as threaded if at least one threading length is longer than the entanglement length N_e. We have chosen this definition because it gives rise to distributions that are independent of the underlying polymer model.[46] The threading properties also vary with the radial position of the ring. In general, the rings closer to the center than $2R/3$ display a higher number of threaded neighbors than the rings at the periphery [Figs. 9(b) and 9(c)], being closer to the bulk values. In Fig. S9, we also show that qualitatively, the same effect is observed for the threshold $R/2$. There, interestingly, the longest central rings display a slightly elevated number of threaded neighbors in comparison to the bulk value. These observations agree with the trend that more expanded rings are in the interior, and the more expanded rings thread more likely.[43] As can be seen in Fig. 9(c), having fewer neighboring rings [Fig. 8(b)] in the case of confinement is related to an overall lower number of threaded neighbors in comparison to the bulk case. Interestingly, for ring lengths up to $N = 800$, the distribution of threaded neighbors is consistent with the one found in the bulk [Fig. 9(a)], despite the fact that the confined rings have fewer neighbors on average [Fig. 8(b)]. This is likely because of the fact that smaller rings on average thread much less than the larger ones, having only 1–2 out of 10 neighbors threaded. Furthermore, for $N = 200$ and $N = 400$, even the outer rings have around eight neighbors, which provides a sufficient number of possibilities to gain 1 or 2 relevant threadings and thus yields marginal differences in the threading statistics. On the other hand, longer rings with $N \geq 800$ that are located close to the wall have significantly reduced possibilities of potential threadings (it even becomes smaller with higher N as the number of neighbors grows with N rather very slowly), and therefore, we observe systematically less threaded neighbors for outer rings, while the statistics for inner rings is not affected substantially. In Fig. 9(d), we report the number of surface piercings, that is, how many times a threading ring pierces the surface of the threaded ring. We consider only piercings that create threading longer than N_e (see Ref. 46). Interestingly, while n_{tn} is, on average, lower in confinement in comparison to bulk, the opposite trend holds for n_p, which suggests that the total piercing number $n_{tn}n_p$ could be a relevant quantity characterizing the free energy penalty for opening the tree-like ring conformations. Initially, n_{tn} grows linearly with N, consistent with findings in Ref. 63, but saturates for longer rings due to the compact conformations and finite number of neighbors.[43] For longer rings, n_{tn} and n_p grow sub-linearly, but their product scales with N. In summary, the threading statistics of rings in confinement is mainly affected by a decreased threading capability of those rings located closer to the wall, as well as by a generally slightly smaller number of neighboring polymer chains. Finally, we confirm in Fig. S9(c) of the supplementary material that the distribution of Q exhibits the same universal behavior as in the bulk with an effective scaling $p(Q) \sim Q^{-1.35}$.[46] The experimentally measured threading in a system of confined semi-flexible rings[32] also exhibits roughly linear scaling of minimal surface area with ring length and the number of piercings of a minimal surface with its area. However, note that rings in that work are only up to two Kuhn segments long and that our estimate of the entanglement length of that system is much shorter than the persistence length in contrast to simulations presented here. We, therefore, do not attempt for a detailed quantitative comparison.

C. Dynamics

We characterize the dynamics of the rings in terms of the mean-square displacements of individual monomers of a chain, g_1, and the rings' center of mass, g_3, as a function of the lag time t,

$$g_1(t) = \frac{1}{T-t}\int_0^{T-t}\frac{1}{N}\sum_i^N\left\langle\left[\mathbf{r}_i(t'+t)-\mathbf{r}_i(t')\right]^2\right\rangle \mathrm{d}t', \quad (7)$$

$$g_3(t) = \frac{1}{T-t}\int_0^{T-t}\left\langle\left[\mathbf{R}(t'+t)-\mathbf{R}(t')\right]^2\right\rangle \mathrm{d}t', \quad (8)$$

where $\mathbf{r}_i(t')$ is the position of the ith monomer belonging to a single ring, $\mathbf{R}(t')$ is the position of the center of mass of a ring at a time t' with respect to the center of mass of the whole system at that time, and T is the total simulation time. The angle brackets in Eqs. (7) and (8) $\langle\cdots\rangle$ stand for averaging over the ensemble of rings. As shown in Fig. 10, the early and intermediate time dynamics is consistent with the bulk results. The g_1 exhibits a subdiffusive regime, $g_1(t) \sim t^{\alpha}$, with the exponent α below 0.4 at early times that later even slows down to around 0.25 for the longest rings, in agreement with the bulk values.[19] The $g_3(t)$ shows exponents ranging from 0.75 for smaller rings with $N = 200$ to approximately 0.67 for the bigger ones ($N = 1600$), in full analogy with those observed in the bulk systems

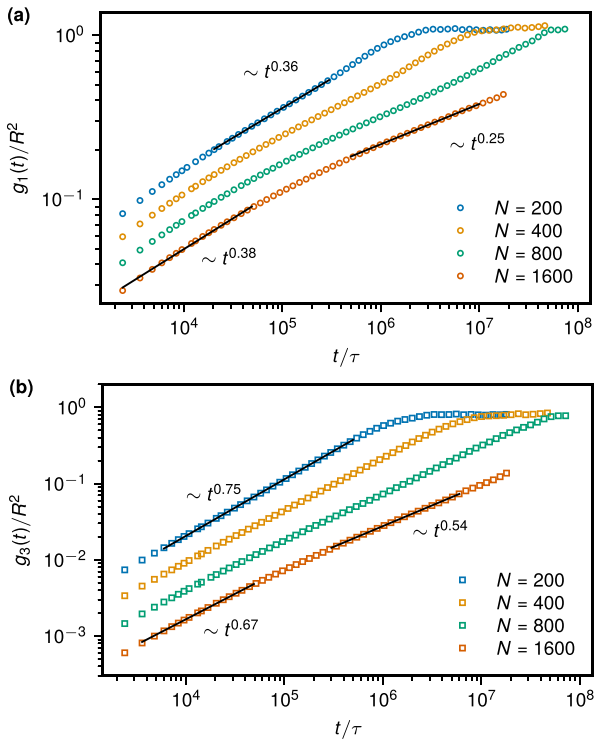

FIG. 10. Mean-square displacements. (a) The mean-square displacements of monomers, g_1, and (b) the rings' center of mass, g_3, as a function of the lag time t. The black solid lines indicate intermediate scaling regimes.

(0.75 for $N = 200$ to 0.65 for $N = 1600$).[18] At the time scale when the bulk system crosses over to diffusion (e.g., $2 \cdot 10^6 \tau$ for $N = 800$), the confined system still subdiffuses. This is because such crossover happens at the scale of $2R_g$ that is comparable to the system size (about $2.5R_g$, as seen in Table I). Here, in contrast, g_3 plateaus due to the confinement, and no intermediate diffusive regime could be observed.

To get a better understanding of the dynamics of the rings within the confining sphere, we separately analyzed the mean-square displacements of the rings' center of mass along the radial direction and perpendicular to it, $g_3^{\parallel}(t)$ and $g_3^{\perp}(t)$, respectively, as a function of the lag time t. To do so, for a time interval $[t', t'+t]$, we first evaluated the ring's displacement along the radial direction, $\boldsymbol{\delta}^{\parallel}(t)$, and perpendicular to it, $\boldsymbol{\delta}^{\perp}(t)$,

$$\boldsymbol{\delta}^{\parallel}(t,t') = \big(\big(R(t'+t) - R(t')\big)\hat{\mathbf{R}}(t'+t), \tag{9}$$

$$\boldsymbol{\delta}^{\perp}(t,t') = \mathbf{R}(t'+t) - \mathbf{R}(t') - \boldsymbol{\delta}^{\parallel}(t), \tag{10}$$

where $R(t')$ is the magnitude the position vector $\mathbf{R}$ at the time t', assuming that $\mathbf{R}$ is measured from the sphere's center, and $\hat{\mathbf{R}} = \mathbf{R}/R$. Consequently, for a fixed lag time t, the displacements in Eq. (9) are squared and averaged over time and over different rings,

$$g_3^{\parallel/\perp}(t) = \frac{1}{T-t}\int_0^{T-t}\left\langle\left[\boldsymbol{\delta}^{\parallel/\perp}(t,t')\right]^2\right\rangle \mathrm{d}t'. \tag{11}$$

Note that with such definition, $\boldsymbol{\delta}^{\perp}(t)$ is a sum of two orthogonal displacements along the ϕ- and θ-directions in the spherical coordinate system, and therefore,

$$g_3(t) = g_3^{\parallel}(t) + g_3^{\perp}(t). \tag{12}$$

Also note that we do not track the cumulative values of the angular components but consider the values of the angles to $\theta \in [0, \pi]$, $\phi \in [0, 2\pi]$, and therefore, the $g_3^{\perp}$ is bounded too. As shown in Fig. 11, the spherical confinement generates an anisotropic behavior of the rings' motion along the different directions. Although both directions exhibit very similar subdiffusive exponents, the angular component dominates $g_3^{\perp}(t)$ over the radial component $g_3^{\parallel}(t)$ by almost an order of magnitude. This emerges due to the inhomogeneous radial density distribution [Fig. 8(a)]. Similar effect, but about factor of two weaker, can be observed for linear chains (not shown), where the density anisotropy is weaker due to their shallower correlation hole.[18] Furthermore, we find that the radial [Fig. 11(a)] and total [Fig. 10(b)] mean-square displacements can be brought on top of each other at longer times if the time axis is multiplied by $N^{-2.4\pm0.1}$, which corresponds to the scaling of the ring's diffusion coefficient in the bulk melts $D \sim N^{-2.3\pm0.1}$,[19] as shown in Fig. S11. Finally, some works quantify the radial dynamics differently, resulting in a different anisotropy and a seeming superdiffusive regime of the radial rings' displacements (see the discussion in the supplementary material).

We further quantify the dynamics in terms of the relaxation of different quantities. First, we consider the structural relaxation proposed recently in Ref. 65 to quantify the effect of threadings

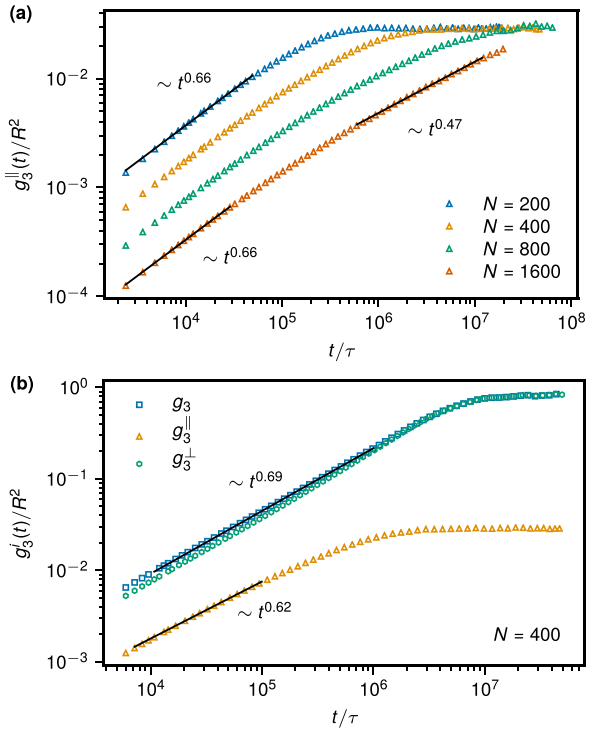

FIG. 11. Anisotropic dynamics within the confining sphere. (a) Radial components of the mean-square displacements for different N. (b) Comparison between different components of g_3 for $N = 400$. Similar results are found for other N (not shown). The black solid lines indicate intermediate scaling regimes.

in ring-linear blends. The relaxation is in terms of the terminal autocorrelation function (TACF) $\langle \mathbf{u}(t) \cdot \mathbf{u}(0) \rangle$, where $\mathbf{u}(t)$ is the unit vector connecting two monomers contourwise $N/2$ apart and the average is performed over all such possible monomers within rings, over different chains and time. The resulting function is shown in Fig. 12(a) with the inset showing the scaling of the corresponding relaxation time with N. The exponent 2.4 is comparable to the one obtained in the bulk (2.2)[19] for a similar structural relaxation quantity computed as the autocorrelation of a vector $\mathbf{c} = \mathbf{u}_1 \times \mathbf{u}_2$, where the two vectors are connecting monomers 0 to $N/2$ and $N/4$ to $3N/4$. In Fig. 12(b), we compare the TACF of rings that are located close to the confining wall to those in the sphere's interior. Such TACF was averaged over time periods when a ring is continuously residing in the respective region. We find that the structural relaxation of inner rings is slowed-down in comparison to the outer ones, which can be attributed to a more pronounced threading in the former region. Unfortunately, due to the lack of long time statistics for the region-resolved TACF, we were not able to accurately estimate the relaxation times in the two regions separately and verify their scaling with N.

Additionally, we quantify the dynamics of the neighbor exchange. We compute the two-point contact correlation function $\hat{\chi}_c(t) = \langle n_{ij}(t_0) n_{ij}(t_0 + t) \rangle_{t_0,ij}$, where $n_{ij}(t)$ is unity if ring i is a neighbor of ring j in the sense of $K_1(a)$ with $a = R_e$ and zero

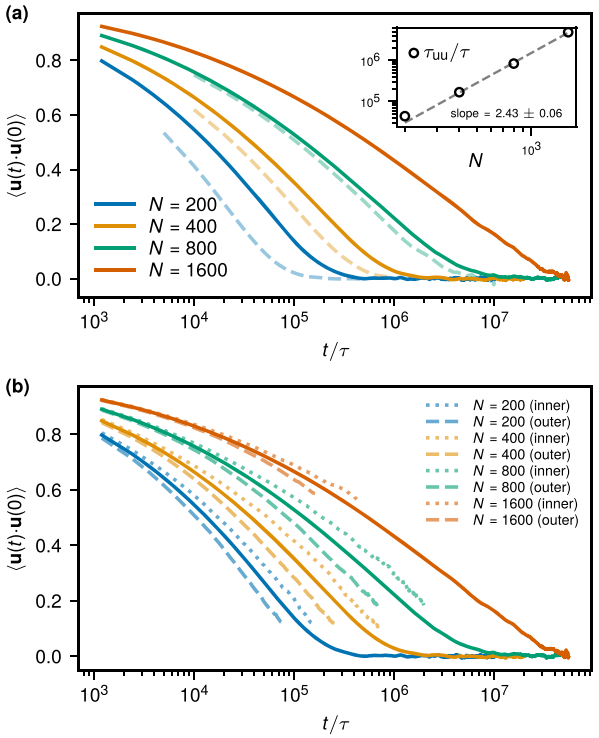

FIG. 12. Terminal autocorrelation functions. (a) TACF of confined rings (solid lines) compared to equivalent bulk systems (dashed lines). Inset: the relaxation time τ_{uu} computed as $\tau_{uu} = \int\langle \mathbf{u}(t)\cdot\mathbf{u}(0)\rangle dt$ as a function of N on a log–log scale. (b) TACF of confined rings averaged over all chains in the system (solid lines) and over those that are located in the inner shell with their center of mass position $r < 2R/3$ (dotted lines) and in the outer shell with $r > 2R/3$ (dashed lines).

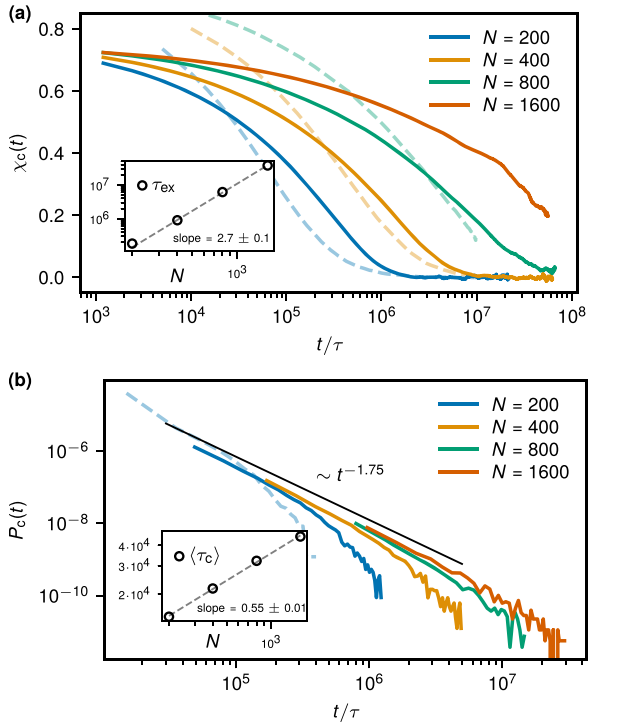

FIG. 13. Neighbor exchange dynamics. (a) The neighbor exchange correlation function $\chi_c(t)$ as a function of time for different ring lengths N. Inset: the mean neighbor exchange time τ_{ex} defined as $\tau_{ex} = \int\chi_c(t)dt$ as a function of N in the log–log scale. To estimate τ_{ex} for $N = 1600$, the tail of $\chi_c(t)$ was extended with a stretched exponential fit. (b) Contact duration distribution P_c for different ring lengths N. The black solid line highlights the scaling regime $P_c(t) \sim t^{-1.75\pm0.01}$. Inset: the mean contact time $\langle \tau_c \rangle$ as a function of N on a log–log scale. The dashed lines in (a) and (b) of the respective color corresponds to the bulk systems of rings.

otherwise [see Fig. 8(b)]. The correlation $\hat{\chi}_c$ is non-vanishing at long times because in a finite system, there is a probability p_n that any two rings are neighbors at any time, which is given by the average number of neighbors of a ring divided by all the possible number of neighbors. Therefore, $p_n = \langle \sum_j n_{ij}(t)\rangle_{t,i}/(M-1)$, where the mean number of neighbors of a ring i is averaged over i and time. In Fig. 13(a), we plot $\chi_c(t) = \hat{\chi}_c(t) - p_n$ as a function of time. Furthermore, from $\chi_c(t)$, we extract the mean exchange time τ_{ex} given by $\tau_{ex} = \int\chi_c(t)dt$. The exchange time τ_{ex} scales with N with the exponent $\simeq 2.7 \pm 0.1$, which is consistent with the exponent found for the relaxation time in the bulk systems.[12,19] The tails of $\chi_c(t)$ can be accurately fit with a stretched exponential $\exp\left(-(t/t_0)^{\beta}\right)$ with $\beta = 0.6$–0.8 (smaller values correspond to larger N). The significant prefactor in this scaling relation makes the exchange time about one order of magnitude larger than the diffusion time in bulk.[19] This behavior arises not only from a neighbor exchange dynamics but also from the finite volume of the enclosing sphere in which the rings frequently meet repeatedly. Such behavior is expected as χ_c is more related to the diffusional properties rather than the structural relaxation. Interestingly, χ_c of the bulk system [dashed line in Fig. 13(a)] decays to zero slightly faster as for the confined case, and its shape is different at early times, suggesting a different process of χ_c relaxation in the two cases. This is illustrated in Fig. 13(b) in which the distribution of contact times $P_c(t)$ is plotted for the bulk case with $N = 200$ and for different N in the confined case. Note that $P_c(t) \sim t^{\alpha/2-2}$ is connected to the distribution of the return times of a random walker with the subdiffusive exponent α[52,66,67] characterizing the dynamics of rings. This agrees well with the subdiffusion of the rings with $\alpha \in [0.5, 0.75]$. The presence of the wall enhances the contact time in the confined case in comparison to bulk, as is clear from the later decay of the P_c [blue solid and dashed lines in Fig. 13(b)]. This explains also the different χ relaxation process. The mean contact time $\langle \tau_c \rangle$ scaling as $\langle \tau_c \rangle \sim N^{0.55}$ grows more slowly with N in comparison to τ_{uu} and τ_{ex}. The scaling exponent of τ_c with N is a consequence of the rings' subdiffusion. The average contact time based on the distribution above is $\langle \tau_c \rangle \sim \lambda^{\alpha/2}$, where λ is a typical time scale characterizing the power-law regime. Then, λ must be proportional to typical relaxation times for rings. The relaxation time scales as $\lambda \sim N^x$, with x being $\simeq 2.4$ in the case of the structural and 2.7 for the diffusional relaxation mechanism, both of which can contribute to the contact breaking events. This gives $\langle \tau_c \rangle \sim N^{x\alpha/2}$, i.e., exponent somewhat above α in either case, in agreement with our findings.

Similar to the neighbor exchange, we analyzed the threading dynamics only for the two shorter systems. We compute the two-point threading correlation as $\hat{\chi}_{\rm th}(t) = \langle n_{ij}(t_0) n_{ij}(t_0 + t)\rangle_{t_0,ij}$, where now the indicator function $n_{ij}(t)$ is unity if ring i threads ring j with $L_{\rm sep} > N_{\rm e}$ and zero otherwise. In full analogy to the neighbor correlation, the $\hat{\chi}_{\rm th}$ is non-vanishing at long times. The probability $p_{\rm th}$ that any two rings are threading at any time is given by the average number of threaded neighbors of a ring $n_{\rm tn}$ divided by all the possible number of neighbors $p_{\rm th} = n_{\rm tn}/(M-1)$. We plot the threading correlation in Fig. 14, and in the inset, we show the distribution of the threading duration $P_{\rm th}(t)$. We find that the longest threading durations are almost an order of magnitude shorter than the relaxation of the threading correlations, and this discrepancy is larger for the longer rings. This could mean that although the duration of each threading is relatively short, it requires a number of correlated threading events to be relaxed in order for a ring to move. Consistent with that is the fact that the threading duration agrees with the structural relaxation (when terminal autocorrelation functions vanish in Fig. 12), and additionally, the neighbor exchange dynamics ($\chi_{\rm c}$) agrees with the threading de-correlation. The former fact contrasts with the bulk findings in Ref. 63, where the structural relaxation is faster than the threading. However, here, we only take into account threadings that are deeper than the entanglement length. When threadings of any depth are considered, we find that the threading state can be maintained by the short threadings for longer time. However, the short threadings do not have impact on the final de-correlation time, which is governed by the deep threadings (see the supplementary material and Fig. S3).

Although the view of the ring relaxation being governed by the correlated sequence of unthreading events is plausible, we cannot rule out that the threading is only a consequence of spatial proximity that is maintained by another mechanism. Specifically, the rings form compact structures with a pronounced correlation hole. As such, rings could be viewed on the scale of $R_{\rm g}$ as soft colloids that, especially in confined space, might require collective mode of relaxation, similar to systems approaching a glass transition. In other words, for a ring to move, others have to rearrange to make space for it, which prolongs the exchange times. The confinement induces an effectively higher density in the center of the volume interior (Fig. S8) and also restricts the possible motion directions at the periphery. Both of these effects would enhance the relaxation times in comparison to the bulk, in agreement with our observation [Fig. 13(a)].

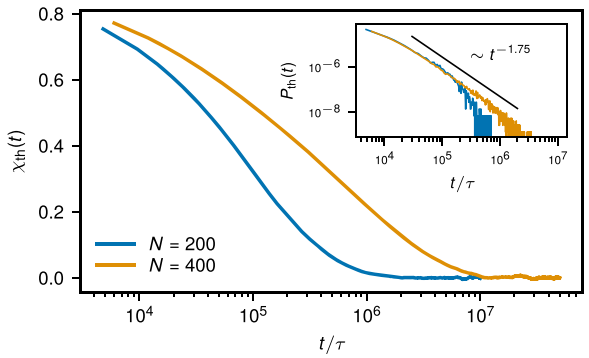

FIG. 14. Threading exchange dynamics. The two time-points threading correlator $\chi_{\rm th}(t)$ for the two systems with $N = 200$ and $N = 400$. Inset: the distribution of threading times $P_{\rm th}(t)$ for these systems. The black solid line highlights the scaling regime $P_{\rm th}(t) \sim t^{-1.75\pm0.01}$.

IV. DISCUSSION AND CONCLUSIONS

We have shown that a small number of spherically confined, unknotted, and non-concatenated rings in melt maintain the universal features of the main static and dynamic characteristics known from the bulk systems.[18,19] Therefore, the connection between the conformational properties of the topologically constrained polymers and the chromatin of higher eukaryotes "survives" the enclosure of the former in the confinement.

The ring conformations at the boundary display γ close to unity despite the fact that a part of the ring has smooth surface ($d_{\rm b} = 2$) and, as such, would be represented by the exponent $\gamma = 2 - (2/3) = 1.33$. This means that the conformations of the confined rings are from the geometrical perspective well represented by space-filling curves that have smooth outer, but fractal inner boundary. Examples of such space-filling curves have been constructed in Refs. 35 and 40. Further work is necessary to unambiguously determine the structure factor and contact probability scaling properties for these "hybrid" space-filling conformations. We hypothesize that this could be relevant when interpreting the scaling of the contact probabilities within different chromatin (epigenomic) domains. If the domain formation is due to different interaction energies (proposed in Ref. 68), the domain boundaries would be governed by minimizing the interfacial area, which would lead to a smooth interface affecting the contact probability of the segment similar to a smooth confining wall. In this context, the comparison of our structural data with the scattering experiments performed on chromatin at the periphery of the nucleus would be very interesting. Indeed, such a system is much more complex than the present simple coarse-grained model, and therefore, the results would also depend on the nature of the interaction of the chromatin with the nuclear lamina. In contrast to our simulations here, recent results conjecture this interaction to be attractive in most cells; however, the rod photoreceptors of nocturnal mammals do not exhibit this attraction and therefore might be good candidates for the tests of our results.[69]

Other differences between the bulk and confined case include radially dependent conformational and threading properties of the rings and the anisotropic dynamics along the directions parallel and perpendicular to the sphere's radius. These effects arise from the confinement-induced radial density variations of the rings as well as their compact structure at melt densities. Despite the threading differences with respect to the bulk, the confinement does not reduce the threading to the extent comparable to the effective tree-like model.[21,46] Therefore, the question of the construction of an effective model of equilibrated ring melt remains open not only in the bulk[46] but also in the confinement.

The confinement in the present work represents one of many recently proposed mechanisms affecting the phase-space of the uncrossable polymers, such as more complex topology,[52] controlled concatenation,[70–74] supercoiling,[75] or activity.[53] Considering the

effects of these perturbations brings the system closer to a practical material or biological situation but also improves our understanding of the unperturbed topologically constrained matter. Considering the activity, recently, it has been shown that a bulk system of non-concatenated rings with active segments can lead to a very slowly relaxing state, the so-called active topological glass.[53] The relaxation is slowed down by the increased number of threadings and their spatial and temporal extent that dramatically differs from the one found in equilibrium ring melts. Such a system possesses many similarities with the chromatin of living cells, such as the slow relaxation, dynamic heterogeneity, and polymer size dependence on the level of the activity. The questions whether such state is possible to create in a confined geometry and whether it is relevant for biological conditions remain open. The results of the present work, however, provide the reference equilibrium values of the observables that the system would originate from.

SUPPLEMENTARY MATERIAL

See the supplementary material for additional information on static and dynamic properties of the considered systems.

AUTHORS' CONTRIBUTIONS

S.M.P. and I.C. contributed equally to this work.

ACKNOWLEDGMENTS

The authors are thankful to C. N. Likos and H.-P. Hsu for fruitful discussions. This work was supported by the European Research Council under the European Union's Seventh Framework Program (Grant No. FP7/2007-2013)/ERC Grant Agreement No. 340906-MOLPROCOMP. J.S. acknowledges support from the Austrian Science Fund (FWF) through the Lise-Meitner Fellowship No. M 2470-N28. The authors acknowledge networking support by the COST Action (Grant No. CA17139). We are grateful for a generous computational time at Vienna Scientific Cluster and Max Planck Computing and Data Facility. This research was supported in part by the National Science Foundation under Grant No. NSF PHY-1748958 and NIH Grant No. R25GM067110. J.S. and K.K. acknowledge the program "Biological Physics of Chromosomes" KITP UCSB, 2020, for providing a discussion forum this work benefited from.

DATA AVAILABILITY

The data that support the findings of this study are available from the corresponding author upon reasonable request.

REFERENCES

[1] P. de Gennes, *Scaling Concepts in Polymer Physics* (Cornell University Press, Ithaca, USA, 1979).
[2] S. F. Edwards, Br. Polym. J. **9**, 140 (1977).
[3] P. G. de Gennes, J. Chem. Phys. **55**, 572 (1971).
[4] F. Ferrari and I. Lazzizzera, Nucl. Phys. B **559**, 673 (1999).
[5] A. R. Khokhlov and S. K. Nechaev, Phys. Lett. A **112**, 156 (1985).
[6] M. E. Cates and J. M. Deutsch, J. Phys. **47**, 2121 (1986).
[7] M. Rubinstein, Phys. Rev. Lett. **57**, 3023 (1986).
[8] A. Y. Grosberg, S. K. Nechaev, and E. I. Shakhnovich, J. Phys. **49**, 2095 (1988).
[9] S. P. Obukhov, M. Rubinstein, and T. Duke, Phys. Rev. Lett. **73**, 1263 (1994).
[10] S. Obukhov, A. Johner, J. Baschnagel, H. Meyer, and J. P. Wittmer, Europhys. Lett. **105**, 48005 (2014).
[11] A. Y. Grosberg, Soft Matter **10**, 560 (2014).
[12] J. Smrek and A. Y. Grosberg, J. Phys.: Condens. Matter **27**, 064117 (2015).
[13] J. Suzuki, A. Takano, T. Deguchi, and Y. Matsushita, J. Chem. Phys. **131**, 144902 (2009).
[14] T. Sakaue, Phys. Rev. Lett. **106**, 167802 (2012).
[15] T. Ge, S. Panyukov, and M. Rubinstein, Macromolecules **49**, 708 (2016).
[16] M. Müller, J. P. Wittmer, and M. E. Cates, Phys. Rev. E **53**, 5063 (1996).
[17] M. Müller, J. P. Wittmer, and M. E. Cates, Phys. Rev. E **61**, 4078 (2000).
[18] J. D. Halverson, W. B. Lee, G. S. Grest, A. Y. Grosberg, and K. Kremer, J. Chem. Phys. **134**, 204904 (2011).
[19] J. D. Halverson, W. B. Lee, G. S. Grest, A. Y. Grosberg, and K. Kremer, J. Chem. Phys. **134**, 204905 (2011).
[20] M. Lang, Macromolecules **46**, 1158 (2013).
[21] A. Rosa and R. Everaers, Phys. Rev. Lett. **112**, 118302 (2014).
[22] A. Narros, C. N. Likos, A. J. Moreno, and B. Capone, Soft Matter **10**, 9601 (2014).
[23] M. Kapnistos, M. Lang, D. Vlassopoulos, W. Pyckhout-Hintzen, D. Richter, D. Cho, T. Chang, and M. Rubinstein, Nat. Mater. **7**, 997 (2008).
[24] S. Goossen, A. R. Brás, W. Pyckhout-Hintzen, A. Wischnewski, D. Richter, M. Rubinstein, J. Roovers, P. J. Lutz, Y. Jeong, T. Chang, and D. Vlassopoulos, Macromolecules **48**, 1598 (2015).
[25] A. R. Brás, R. Pasquino, T. Koukoulas, G. Tsolou, O. Holderer, A. Radulescu, J. Allgaier, V. G. Mavrantzas, W. Pyckhout-Hintzen, A. Wischnewski, D. Vlassopoulos, and D. Richter, Soft Matter **7**, 11169 (2011).
[26] A. R. Brás, S. Goossen, M. Krutyeva, A. Radulescu, B. Farago, J. Allgaier, W. Pyckhout-Hintzen, A. Wischnewski, and D. Richter, Soft Matter **10**, 3649 (2014).
[27] S. Goossen, A. Brás, M. Krutyeva, M. Sharp, P. Falus, A. Feoktystov, U. Gasser, A. Wischnewski, and D. Richter, Phys. Rev. Lett. **113**, 168302 (2014).
[28] D. Vlassopoulos, Rheol. Acta **55**, 613 (2016).
[29] T. Iwamoto, Y. Doi, K. Kinoshita, Y. Ohta, A. Takano, Y. Takahashi, M. Nagao, and Y. Matsushita, Macromolecules **51**, 1539 (2018).
[30] T. Iwamoto, Y. Doi, K. Kinoshita, A. Takano, Y. Takahashi, E. Kim, T.-H. Kim, S.-I. Takata, M. Nagao, and Y. Matsushita, Macromolecules **51**, 6836 (2018).
[31] M. Kruteva, J. Allgaier, M. Monkenbusch, L. Porcar, and D. Richter, ACS Macro Lett. **9**, 507 (2020).
[32] L. R. Gómez, N. A. García, and T. Pöschel, Proc. Natl. Acad. Sci. U. S. A. **117**, 3382 (2020).
[33] A. Grosberg, Y. Rabin, S. Havlin, and A. Neer, Europhys. Lett. **23**, 373 (1993).
[34] E. Lieberman-Aiden, N. L. van Berkum, L. Williams, M. Imakaev, T. Ragoczy, A. Telling, I. Amit, B. R. Lajoie, P. J. Sabo, M. O. Dorschner, R. Sandstrom, B. Bernstein, M. A. Bender, M. Groudine, A. Gnirke, J. Stamatoyannopoulos, L. A. Mirny, E. S. Lander, and J. Dekker, Science **326**, 289 (2009).
[35] J. Halverson, J. Smrek, K. Kremer, and A. Grosberg, Rep. Prog. Phys. **77**, 022601 (2014).
[36] A. Rosa and R. Everaers, PLoS Comput. Biol. **4**, e1000153 (2008).
[37] A. Rosa, M. Di Stefano, and C. Micheletti, Front. Mol. Biosci. **6**, 127 (2019).
[38] M. V. Imakaev, K. M. Tchourine, S. K. Nechaev, and L. A. Mirny, Soft Matter **11**, 665 (2015).
[39] J. Smrek and A. Y. Grosberg, Physica A **392**, 6375 (2013).
[40] Z. Benková and P. Cifra, Macromolecules **45**, 2597 (2012).
[41] Z. Benková, P. Námer, and P. Cifra, Soft Matter **12**, 8425 (2016).
[42] I. Chubak, E. Locatelli, and C. N. Likos, Mol. Phys. **116**, 2911 (2018).
[43] J. Smrek and A. Y. Grosberg, ACS Macro Lett. **5**, 750 (2016).
[44] D. Michieletto, D. Marenduzzo, E. Orlandini, G. P. Alexander, and M. S. Turner, ACS Macro Lett. **3**, 255 (2014).
[45] D. Michieletto, D. Marenduzzo, E. Orlandini, G. P. Alexander, and M. S. Turner, Soft Matter **10**, 5936 (2014).
[46] J. Smrek, K. Kremer, and A. Rosa, ACS Macro Lett. **8**, 155 (2019).

[47]E. Lee, S. Kim, and Y. Jung, Macromol. Rapid Commun. **36**, 1115 (2015).
[48]D. Michieletto and M. S. Turner, Proc. Natl. Acad. Sci. U. S. A. **113**, 5195 (2016).
[49]D. Michieletto, Soft Matter **12**, 9485 (2016).
[50]D. Michieletto, N. Nahali, and A. Rosa, Phys. Rev. Lett. **119**, 197801 (2017).
[51]E. Lee and Y. Jung, Polymers **11**, 516 (2019).
[52]A. Rosa, J. Smrek, M. S. Turner, and D. Michieletto, ACS Macro Lett. **9**, 743 (2020).
[53]J. Smrek, I. Chubak, C. N. Likos, and K. Kremer, Nat. Commun. **11**, 26 (2020).
[54]K. Kremer and G. S. Grest, J. Chem. Phys. **92**, 5057 (1990).
[55]R. Everaers, S. K. Sukumaran, G. S. Grest, C. Svaneborg, A. Sivasubramanian, and K. Kremer, Science **303**, 823 (2004).
[56]S. Plimpton, J. Comput. Phys. **117**, 1 (1995), http://lammps.sandia.gov.
[57]N. Ganai, S. Sengupta, and G. I. Menon, Nucleic Acids Res. **42**, 4145 (2014).
[58]J. P. Wittmer, H. Meyer, A. Johner, S. Obukhov, and J. Baschnagel, J. Chem. Phys. **139**, 217101 (2013).
[59]J. D. Halverson, W. B. Lee, G. S. Grest, A. Y. Grosberg, and K. Kremer, J. Chem. Phys. **139**, 217102 (2013).
[60]A. Narros, A. J. Moreno, and C. N. Likos, Soft Matter **6**, 2435 (2010).
[61]A. Narros, A. J. Moreno, and C. N. Likos, Biochem. Soc. Trans. **41**, 630 (2013).
[62]J. Dzubiella, H. M. Harreis, C. N. Likos, and H. Löwen, Phys. Rev. E **64**, 011405 (2001).
[63]D. G. Tsalikis, V. G. Mavrantzas, and D. Vlassopoulos, ACS Macro Lett. **5**, 755 (2016).
[64]W.-C. Lo and M. S. Turner, Europhys. Lett. **102**, 58005 (2013).
[65]A. F. Katsarou, A. J. Tsamopoulos, D. G. Tsalikis, and V. G. Mavrantzas, Polymers **12**, 752 (2020).
[66]G. M. Molchan, Commun. Math. Phys. **205**, 97 (1999).
[67]R. Metzler, G. Oshanin, S. Redner, J.-H. Jeon, A. V. Chechkin, and R. Metzler, *First-Passage Phenomena and Their Applications* (World Scientific, 2014), Vol. 3, p. 175.
[68]D. Jost and C. Vaillant, Nucleic Acids Res. **46**, 2252 (2018).
[69]M. Falk, Y. Feodorova, N. Naumova, M. Imakaev, B. R. Lajoie, H. Leonhardt, B. Joffe, J. Dekker, G. Fudenberg, I. Solovei, and L. A. Mirny, Nature **570**, 395 (2019).
[70]Q. Wu, P. M. Rauscher, X. Lang, R. J. Wojtecki, J. J. de Pablo, M. J. A. Hore, and S. J. Rowan, Science **358**, 1434 (2017).
[71]P. M. Rauscher, S. J. Rowan, and J. J. de Pablo, ACS Macro Lett. **7**, 938 (2018).
[72]Z. Ahmadian Dehaghani, I. Chubak, C. N. Likos, and M. R. Ejtehadi, Soft Matter **16**, 3029 (2020).
[73]P. M. Rauscher, K. S. Schweizer, S. J. Rowan, and J. J. de Pablo, Macromolecules **53**, 3390 (2020).
[74]P. M. Rauscher, K. S. Schweizer, S. J. Rowan, and J. J. de Pablo, J. Chem. Phys. **152**, 214901 (2020).
[75]K. R. Peddireddy, M. Lee, Y. Zhou, S. Adalbert, S. Anderson, C. M. Schroeder, and R. M. Robertson-Anderson, Soft Matter **16**, 152 (2020).